Defects and polaronic electron transport in Fe_2WO_6

Raphael Schuler, Truls Norby, Helmer Fjellvåg
raphael.schuler@smn.uio.no
truls.norby@kjemi.uio.no
helmer.fjellvag@kjemi.uio.no
Department of Chemistry, Centre for Materials Science and Nanotechnology, University of Oslo, POB 1126 Blindern, NO-0318 Oslo

Abstract

We report the synthesis of phase pure Fe_2WO_6 and its structural characterization by high quality synchrotron x-ray powder diffraction, followed by studies of electric and thermoelectric properties as a function of temperature (200 – 950°C) and pO_2 (1 – 10^{-3} bar). The results are shown to be in accordance with a defect chemical model comprising formation of oxygen vacancies and charge compensating electrons at high temperatures. The standard enthalpy and entropy of formation of an oxygen vacancy and two electrons in Fe_2WO_6 are found to be 113(5) kJmol^{-1} and ca. 41(5) Jmol^{-1}K^{-1}, respectively. Electrons residing as Fe^{2+} in the Fe^{3+} host structure act as charge carriers in a small polaron conducting manner. A freezing-in of oxygen vacancies below approximately 650°C results in a region of constant charge carrier concentration, corresponding to an iron site fraction of $X_{Fe^{2+}} \cong 0.03$. By decoupling of mobility from conductivity, we find a polaron hopping activation energy of 0.34(1) eV and a charge mobility pre-exponential u_0 = 400(50) cm^{2}KV^{-1}s^{-1}. We report thermal conductivity for the first time for Fe_2WO_6. The relatively high conductivity, large negative Seebeck coefficient and low thermal conductivity make Fe_2WO_6 an interesting candidate as n-type thermoelectric in air, for which we report a maximum zT of 0.027 at 900°C.

Introduction

Transition metal (TM) tungstates have received increasing scientific interest over the last decade due to possible applications in catalysis, supercapacitors and multiferroics.[1-3] Whereas the divalent TM tungstates (MWO_4) have been investigated intensively, the trivalent TM variants (M_2WO_6) remain largely unexplored. Nevertheless, due to its semiconducting

nature, Fe_2WO_6 is of special interest. Its small bandgap (1.8 eV), relatively high electrical conductivity ($\sigma_{rt} \approx 0.02$ Scm^{-1}), and absorption in the visible light spectrum, make Fe_2WO_6 a candidate for photoanodes in photoelectrochemical cells.[4] The relatively high electrical conductivity is attributed to small polaron electrons that may be seen as Fe^{2+} states hopping along host Fe^{3+} zigzag chains. The crystal structure can be described as a superstructure variant of the α-PbO type (space group *Pbcn)* with unit cell parameters *a* = 4.578, *b* = 16.757, and *c* = 4.968 Å. The structure consists of zigzag chains of edge sharing WO_6 and FeO_6 octahedra along [001]. Bharati *et al.* reported a large positive Seebeck coefficient, indicating p-type conductivity.[5] However, several other publications have rather reported n-type conductivity. In this work, we provide an experimental assessment of defect chemical and electrical transport properties, providing a model of the origin and transport of charge carriers. Specifically, we address these question by first synthesizing phase pure samples of Fe_2WO_6 for which detailed crystallographic information, including possible vacancies at oxygen sites, is deduced from Rietveld refinement of high quality synchrotron x-ray powder diffraction data. By means of careful conductivity, and Seebeck coefficient measurements over a wide range of temperature and oxygen partial pressure, we clearly prove that Fe_2WO_6 is an n-type material. In order to support the findings from diffraction and electrical studies concerning the likeliness of oxygen vacancies being a cause for the interesting transport properties, XPS studies are undertaken for clarifying the potential presence of reduced Fe^{2+} species, that could act as charge carriers in a polaron hopping manner. To our knowledge, there exist no studies on thermal conductivity of Fe_2WO_6 in the literature so far, and we are the first ones to report this property. Our findings indicate a potential relevance of Fe_2WO_6 for high temperature thermoelectric applications. The field of thermoelectric oxides has yet to find a suitable n-type material, able to compete with the unmatched performance of the layered cobaltite p-type $Ca_3Co_4O_9$. With just a few systems showing promising results, e.g. TiO_2, $CaMnO_3$ and ZnO, the discovery of new high temperature stable n-type thermoelectric oxides is a valuable contribution in the search for better materials.

Experimental

Powder samples of Fe_2WO_6 were synthesized using standard solid-state reaction techniques. Stoichiometric amounts of the starting materials Fe_2O_3 (STREM chemicals 99.8%), and WO_3 (Sigma Aldrich 99.9%) were mixed, thoroughly ground in an agate mortar and pressed into 10 mm pellets with a cylindrical die. The pellets were reacted at 950°C for 16 hours in a covered alumina crucible. The pellets were reground and the procedure repeated until a single-phase product was confirmed by powder X-ray diffraction (XRD). Disk shaped pellets were produced

by uniaxial pressing and sintering at 1100°C for 6 hours in air. In house XRD measurements were obtained on a Bruker D8 Discover with CuKα1 radiation, Ge (111) Johanssen monochromator and a Lynxeye detector. High-resolution powder XRD patterns were measured at BM31 (SNBL) at ESRF (France), λ = 0.4943 Å using a Dexela 2923 CMOS two-dimensional detector. Structure refinement was carried out according to the Rietveld method using the TOPAS V5 software. Peak shapes were fitted using a pseudo Voigt peak shape. Corrections applied to the pattern included a second order Chebyshev polynomial, a broad background peak at $2\Theta = 7.5^{o}$ and a cylindrical 2Θ correction term for the capillary geometry. A total of 39 independent parameters were used in the refinement for a total of 427 Bragg reflections in the range $4 \leq 2\Theta \leq 37^{o}$.

Electrical conductivity and Seebeck coefficients were measured at high temperatures in a tube furnace with a custom-built assembly mounted setup in a ProboStat™ cell (NORECS AS, Oslo, Norway). [6] The disc shaped pellets were placed on an alumina plate with an integrated S-type thermocouple. Four Pt-electrodes were pressed on the top surface of the pellets in a van der Pauw geometry by springload. Two additional thermocouples made of 0.2 mm Pt and Pt/10Rh wire were pressed to the top surface of the pellet at a 6-8 mm distance. A resistive heater next to the sample provided a temperature difference of 4-6°C across the sample. The setup allowed simultaneous measurement of in-plane Seebeck coefficient and in-plane conductivity under identical experimental conditions. A custom gas mixer with several O_2 + Ar dilution stages controlled the oxygen partial pressure. The sample was equilibrated at each of the selected oxygen partial pressures for 48 hours whereupon the Seebeck coefficient and conductivity data were measured.

Thermal conductivity was measured by the laser flash analysis method on a Netzsch LFA 457 MicroFLASH from 25°C to 1000°C in nitrogen flow. The graphite coated disk sample was irradiated with laser pulse lengths of 0.5 ms and a Netzsch Pyroceram standard sample was used to determine the specific heat. At 100°C intervals, 3 measurements were taken at each temperature point, of which the mean value was determined.

Thermogravimetric analysis was carried out on a Netzsch TA 449 F1 Jupiter with a sample powder weight of 0.861 mg in an aliumina crucible. In order to reproduce the conditions of the conductivity measurements as precisely as possible, the chamber was flushed with 40 ml/min of synthetic air during the experiment and the same heating rate of 1 °C/min was set between 50°C and 950°C.

X-ray photoelectron spectroscopy (XPS) data was collected on a ThermoFisher Scientific Thetaprobe, with energy scale calibration relative to the Ag $3d_{5/2}$ peak at 368.21 eV and with

the stage polarized to -16 V during experiments. XPS measurements were performed on freshly fractured surfaces of densely sintered pellets of Fe_2WO_6. Data analysis was carried out using CasaXPS software.[7] The spectra were corrected for Shirley backgrounds. Symmetric peaks were fitted using a Voigt peak shape (GL(50)). Asymmetric peaks were fitted using an asymmetric Lorenzian.

Results

The obtained fit to the synchrotron powder XRD pattern of Fe_2WO_6 is shown in Figure 1. The Rietveld refinement analysis confirmed a single phase sample of Fe_2WO_6, crystallizing in space group *Pbcn.* There is no indication for any presence of secondary phases. In the refinement process, the occupancy of the W-site was fixed to 1.00. The results show complete occupation of all other sites except for the O3 site. Unit cell dimensions, atomic coordinates, occupancies and isotropic temperature factors are displayed in Table 1. The refinement converged to R_{wp}= 9.035, R_p = 7.121 (R_{exp}-value and goodness-of-fit are not relevant owing to the 2D detector statistics).[8] The structure consists of WO_6 and FeO_6 octahedra which form edge sharing chains in along [001] and corner sharing along [100] and [010]. The Fe1 site belongs to the chains solely consisting of FeO_6 octahedra, whereas the chains containing the Fe2 site consist of alternating WO_6 and FeO_6 octahedra. The refinements indicate a presence of vacancies at the O3 site. Both the O1 and O2 anions are exclusively linking Fe2-W-Fe2 and Fe1-W-Fe1 octahedra, respectively. On the other hand, the O3 site connects the Fe1 and Fe2 sites, thereby providing linkage to the pure FeO_6 and the alternating WO_6-FeO_6 chains. The occupation refinement points towards a stoichiometry of $Fe_2WO_{5.96}$, but the quantification of the oxygen under-stoichiometry is accompanied by considerable uncertainty (as seen by the calculated standard deviations), owing to the light oxygen atoms (Nb. 8) compared to the electron rich tungsten (Nb. 74). High quality neutron diffraction data appears required to provide more accurate determination of the non-stoichiometry at the O-sites.

Table 1: Crystallographic data for Fe_2WO_6 derived by Rietveld refinement of synchrotron powder X-ray diffraction data, space group *Pbcn*; *a* = 4.5607(1), *b* = 16.6938(4) and *c* = 4.9493(1)Å, (*Z* = 4). Calculated standard deviations in parentheses.

Atom	Multipl.	*x*	*y*	*z*	*Occ.*	*Beq.*
O1	8	0.232(2)	0.2065(8)	0.069(2)	1.00(4)	0.60(18)
O2	8	0.257(2)	0.0393(7)	0.108(3)	1.00(4)	0.60(18)
O3	8	0.282(2)	0.3724(10)	0.074(2)	0.98(2)	0.60(18)
W	4	0	0.11211(8)	0.25	1	1.59(3)
Fe1	4	0	0.44424(17)	0.25	1.000(9)	0.19(5)
Fe2	4	0	0.77651(19)	0.25	1.000(8)	0.19(5)

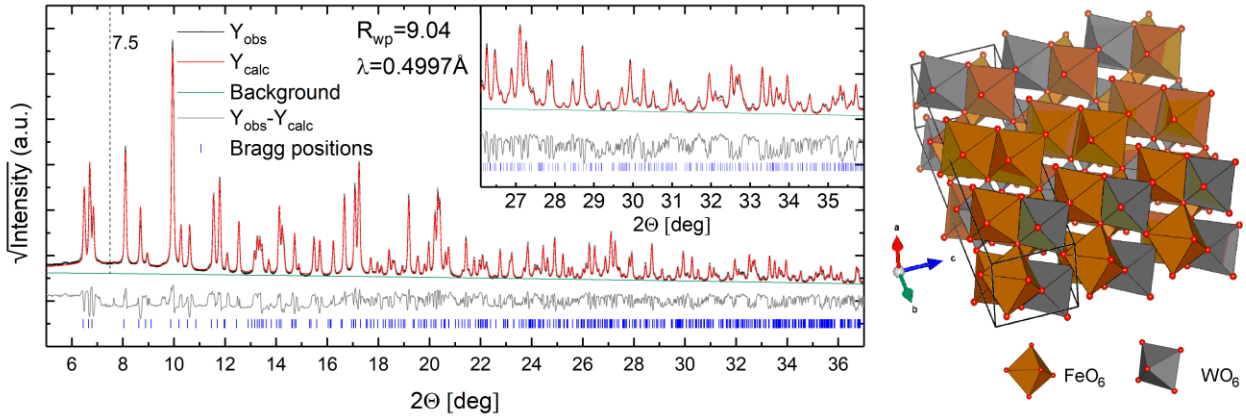

Figure 1: Synchrotron x-ray powder diffraction pattern of Fe_2WO_6 with zoomed high angle region (inset). The intensity is displayed as square root to help emphasize weak reflections. The broad fitted background peak is marked by the dotted line at 2Θ = 7.5º.

Figure 2a shows the Seebeck coefficient as a function of inverse temperature. It remains large and negative with two recognizable regions, delimited at about 650°C. The decrease in magnitude of the Seebeck coefficient at higher temperatures indicates an increasing charge carrier concentration whereas the low temperature range indicates a constant charge carrier concentration as seen by an almost constant Seebeck coefficient. Noteworthy, the Seebeck data reported by Bharati *et al.* has similar absolute values, but of positive sign. Hence, they discuss their findings under the assumption that holes are the dominant charge carriers. Support to the present findings is provided by various reports on n-type conductivity from qualitative Seebeck measurements.[9, 10] The electrical conductivity as a function of inverse temperature is shown in Figure 2b. The conductivity increases with temperature in a thermally activated manner, depicting two straight lines in the logarithmic plot, with a change in slope around 650°C, coinciding with the transition in the Seebeck coefficient.

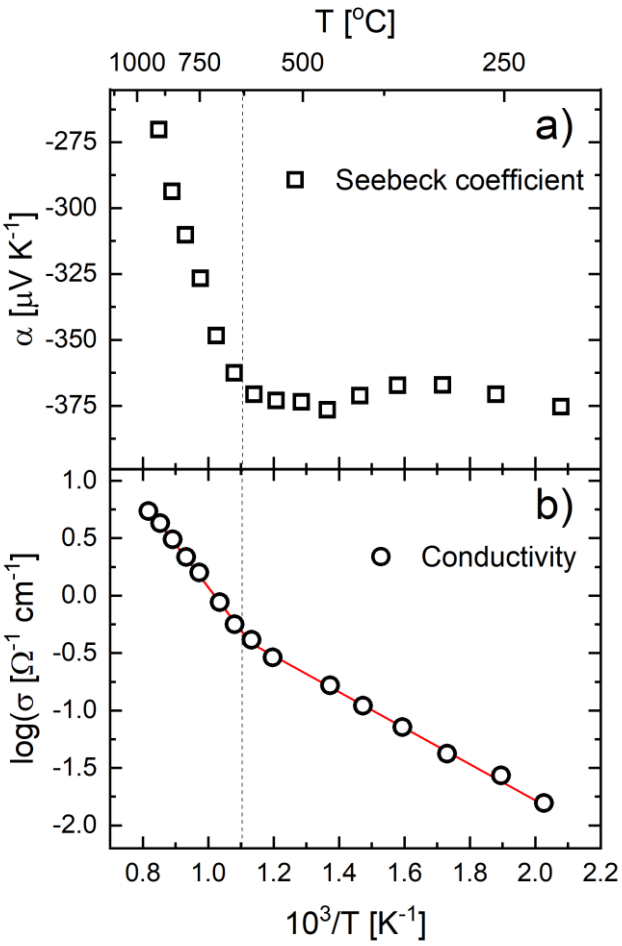

Figure 2: Inverse temperature dependence of a) Seebeck coefficient and b) conductivity of Fe_2WO_6 in air.

The thermal conductivity of Fe_2WO_6, depicted in Figure 3 is no strong function of temperature, despite some fluctuation, and shows a declining trend with increasing temperature, reaching a minimum of 1.25 $Wm^{-1}K^{-1}$ at 600°C. The low thermal conductivity can be attributed to the low dimensionality of the structure and large unit cell.

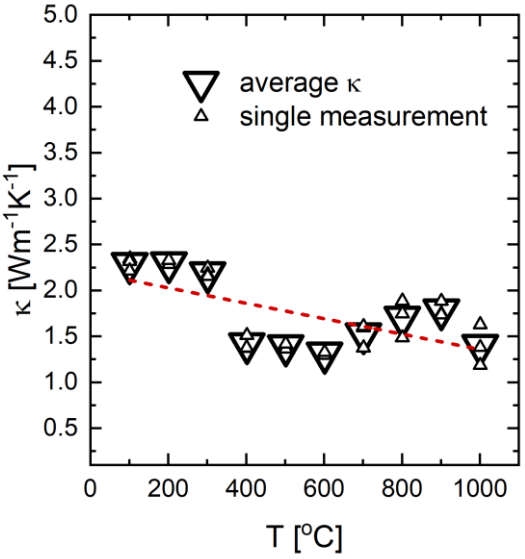

Figure 3 Thermal conductivity determined by Laser Flash Analysis. The dotted line is a guide to the eye indicating the decreasing trend.

It has been suggested that oxygen non-stoichiometry may play an important role in Fe_2WO_6, but to our knowledge there are no detailed studies at hand.[11] Thermogravimetric analysis in air, depicted in Figure 4, shows a nearly constant sample weight below 600°C with minor fluctuations, attributed to buoyance of the scale. Above 650°C a close to linear weight loss can be observed, followed by an equivalent weight gain during the cooling process, flattening out below about 600°C with a slight hysteresis.

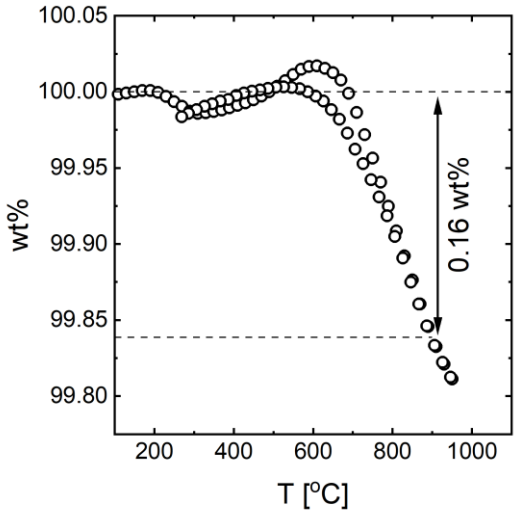

Figure 4 Thermogravimetric analysis of Fe_2WO_6 in air during heating and cooling ramps of 1°C /min in accordance with the conductivity and thermopower measurements. The weight loss from the baseline to 900°C is indicated.

Figure 5 shows the electrical conductivity and charge carrier concentration from Seebeck coefficient measurements at various oxygen partial pressures, and measured simultaneously at 750°C. For consistency, the charge carrier concentration is expressed as Fe^{2+} site fraction obtained from the Seebeck coefficient, which will be discussed later. The dependency remains negative over the investigated p_{O_2} region, with a slope of the order of -1/6 for both conductivity and charge carrier concentration, as expected for non-stoichiometry dominated by oxygen vacancies.

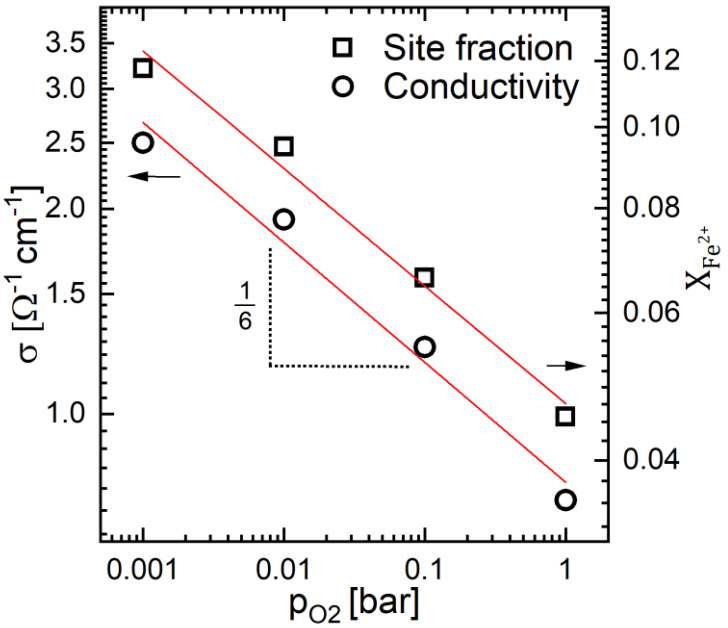

Figure 5: Brouwer diagram showing logarithmic conductivity and charge carrier concentration given as Fe^{2+} site fraction, obtained from Seebeck measurements, as function of oxygen partial pressure. The data were collected isothermally at 750°C. Both datasets show slopes of around -1/6.

Figure 6a shows a narrow scan of the iron 2p region of the X-ray photoelectron (XPS) spectrum of Fe_2WO_6 at room temperature. The two well separated spin-orbit features $2p_{3/2}$ and $2p_{1/2}$ at 710.8 eV and 724.4 eV are visible. The typical Fe^{3+} satellite peak at 719.39 eV is clearly distinguishable and shows the typical shift of 8.6 eV towards higher binding energies. The intensity ratio between the $2p_{1/2}$ and $2p_{3/2}$ peaks matches closely the ratio of 1:2 (1:1.994), which is typical for Fe_2O_3. This indicates that the Fe^{3+} atoms in Fe_2WO_6 have similar electronic properties as in Fe_2O_3.[12] However, the Fe $2p_{3/2}$ peak is fitted insufficiently when using only one component. Figure 6a shows an additional shoulder at low binding energy and a weak, broad feature at higher binding energy. The latter feature is attributed to a surface signal, similar to what has been reported for Fe_2O_3.[12] Surface peaks are considered to arise for a freshly cleaved surface that leaves atoms at the surface with a reduced coordination.[13, 14]

The shoulder at lower binding energy is typical for FeO and Fe^{2+} containing compounds and is taken as an indication of the presence of Fe^{2+} species in the Fe^{3+} host structure. The presence of Fe^{2+} species in Fe_2WO_6 has been discussed in earlier literature.[15] The area ratio between the Fe 2p peaks of Fe^{3+} and the Fe^{2+} shoulder indicates a site fraction of approximately 0.03 (see Table 2). It appears that Fe_2WO_6 in this way behaves quite similar to its Fe^{2+} sister compound $FeWO_4$ which in turn has been found to host small amounts of Fe^{3+} as (p-type, hole) conducting species.[16]

Table 2: Parameters derived from fitting of XPS data for the Fe 2p, W 4f and reference Ag 3d peak regions.

Signal	Position (eV)	FWHM (eV)	Area
Fe $2p_{3/2}$	710.80	2.63	4066
Fe $2p_{1/2}$	724.39	4.09	2839
Fe^{3+} satellite	719.40	1.99	357
Fe^{2+} shoulder	709.87	0.68	256
Surface peak	713.33	2.44	1340
W $4f_{7/2}$	35.32	0.86	4367
W $4f_{5/2}$	37.46	0.87	3339
Ag $3d_{5/2}$	368.21	0.55	29839

Figure 6b shows an XPS narrow scan for the tungsten 4f region. The $4f_{7/2}$ and $4f_{5/2}$ spin orbit peaks were fitted with symmetric Voigt functions and are located at 35.3 eV and 37.4 eV, split by 2.14 eV. The intensity ratio of 1:1.308 closely matches the typical f subshell ratio of 3:4. These XPS data show close resemblance to those of WO_3 with W^{6+} in fully oxidized state. No sign of any shoulder at lower binding energies is visible, which would be indicative of tungsten in a lower oxidation state. Peak positions, FWHM, and integrated area are summarized in Table 2.

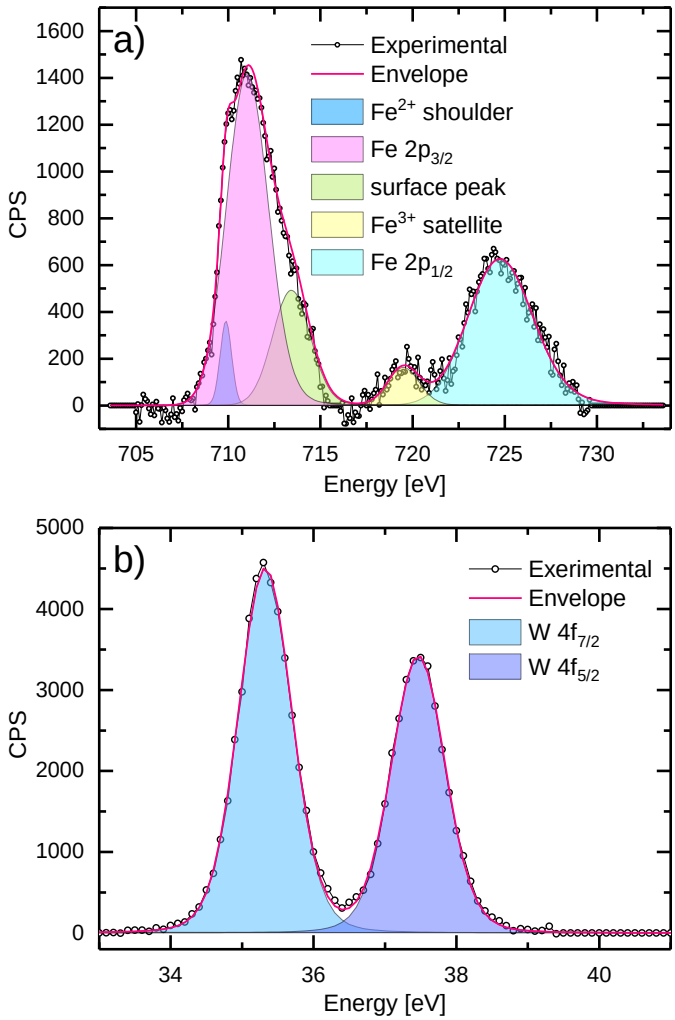

Figure 6: Shirley background subtracted close up X-ray photoelectron spectra of a) Fe 2p and b) W 4f signals in Fe_2WO_6.

Discussion

The n-type conductivity in Fe_2WO_6 can be assigned to mixed iron valence with Fe^{2+} species being the active conducting species hopping along the Fe^{3+} host sites. We make use of the modified Heikes formula for transition metal oxides, containing the degeneracy factors of the valence states, to estimate the charge carrier concentration from the Seebeck coefficient.[17, 18]

$$\alpha = -\frac{k_B}{e} ln\left(\frac{g_{Fe^{3+}}}{g_{Fe^{2+}}}\frac{(1 - X_{Fe^{2+}})}{X_{Fe^{2+}}}\right) \quad (1)$$

Here, α is the Seebeck coefficient, k_B the Boltzmann constant, e the elemental charge, and $X_{Fe^{2+}}$ denotes the number of Fe^{2+} per iron site $\left(X_{Fe^{2+}} = \frac{[Fe^{2+}]}{[Fe^{3+}]+[Fe^{2+}]}\right)$. The factors $g_{Fe^{2+}}$ and $g_{Fe^{3+}}$ take into account the degeneracies for Fe^{2+} and Fe^{3+} states. In Fe_2WO_6, Fe^{3+} exists in

the non-degenerate d^5_{hs} configuration with spin 5/2, and thus the degeneracy factor is $g_{Fe^{3+}} = 6$. Fe^{2+} has been shown to exist in d^6_{hs} state in both FeO and $FeWO_4$ and is expected to keep the high spin configuration of $(t_{2g}\uparrow^3)(t_{2g}\downarrow^1)(e_g\uparrow^2)$ in Fe_2WO_6 as well. The large crystal field splitting leaves the sixth d electron to enter the lower lying, triply degenerate ($t_{2g}\downarrow$) orbital, with a total spin of 2, the degeneracy factor is thus given by $g_{Fe^{2+}} = 15$. [19, 20] The site fraction calculated accordingly from Seebeck data is shown in Figure 7 and decreases towards lower temperatures until it becomes almost constant below 650°C with a value of $X_{Fe^{2+}} \cong 0.031$–0.034, corresponding to a charge carrier concentration of approximately 6.9(5) × 10^{20} cm^{-3}. In the following, we will refer to these two regions as the equilibrium and frozen-in regions.

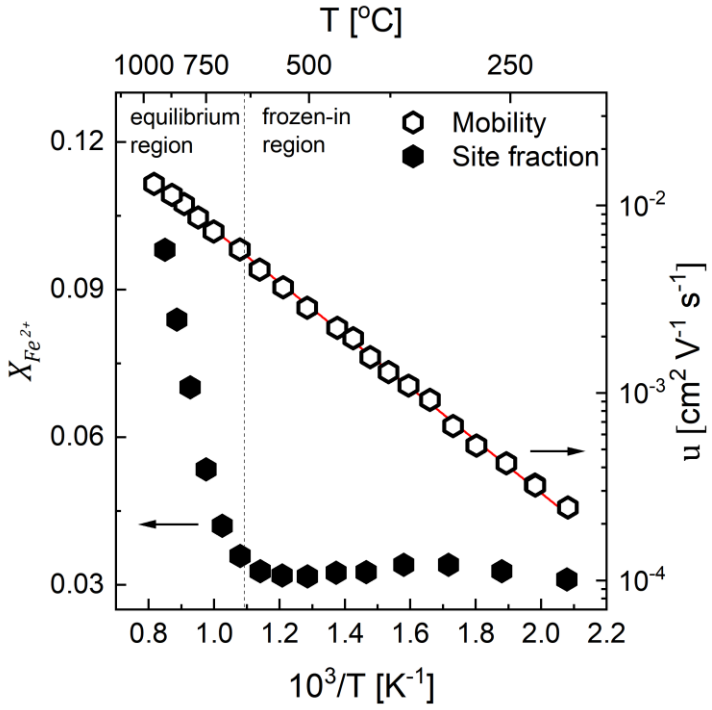

Figure 7: Site fraction ($X_{Fe^{2+}}$) of Fe^{2+} in Fe_2WO_6 obtained from Heikes formula and charge carrier mobility (u) obtained from combination with conductivity data. The dotted line indicates transition from the equilibrium region to the frozen-in region around 650°C.

The temperature dependent site fraction of Fe^{2+} as deduced from the Seebeck data and the oxygen non-stoichiometry data derived from XRD and XPS data are in good overall agreement taking the accuracies of the methods and analyses into account. The room temperature XRD data suggest that the oxygen vacancies occur only at one of the three oxygen sites (O3). We assume that this situation is maintained also at high temperatures. Since there are two O3 atoms and two Fe atoms per Fe_2WO_6 formula unit, the electroneutrality condition for electrons (i.e. Fe^{2+}) that are charge compensating the oxygen vacancies at the O3-site can be expressed as site fractions according to Kröger-Vink notation as

$$X_{\mathrm{Fe^{2+}}} = 2X_{v_{O3}^{\bullet\bullet}} \tag{2}$$

The formation of O3 oxygen vacancies and Fe^{2+} species reads

$$2Fe_{Fe}^{x} + O_{O3}^{x} = v_{O3}^{\bullet\bullet} + 2Fe_{Fe^{3+}}^{2+\prime} + \frac{1}{2}O_2 \tag{3}$$

The equilibrium coefficient, including the electron degeneracy is given by

$$K_{v_{O3}^{\bullet\bullet}} = \frac{a_{v_{O3}^{\bullet\bullet}} \left(g_{\mathrm{Fe^{2+}}}\, a_{Fe_{Fe^{3+}}^{2+\prime}}\right)^2}{a_{O_{O3}^{x}} \left(g_{\mathrm{Fe^{3+}}}\, a_{Fe_{Fe}^{x}}\right)^2} p_{O_2}^{\frac{1}{2}} = \frac{[v_{O3}^{\bullet\bullet}] \left(g_{\mathrm{Fe^{2+}}} \left[Fe_{Fe^{3+}}^{2+\prime}\right]\right)^2}{[O_{O3}^{x}](g_{\mathrm{Fe^{3+}}}[Fe_{Fe}^{x}])^2} p_{O_2}^{\frac{1}{2}} \tag{4}$$

In the approximation of small defect concentrations we can express the oxygen vacancy and Fe^{2+} concentrations as site fractions and the equilibrium coefficient simplifies to

$$K_{v_{O3}^{\bullet\bullet}} = X_{v_{O3}^{\bullet\bullet}} \left(\frac{g_{\mathrm{Fe^{2+}}}}{g_{\mathrm{Fe^{3+}}}}\right)^2 (X_{\mathrm{Fe^{2+}}})^2 p_{O_2}^{\frac{1}{2}} \tag{5}$$

By assuming the electroneutrality condition (2) equation (5) can be rearranged to

$$X_{\mathrm{Fe^{2+}}} = (2K_{v_{O3}^{\bullet\bullet}})^{\frac{1}{3}} \left(\frac{g_{\mathrm{Fe^{2+}}}}{g_{\mathrm{Fe^{3+}}}}\right)^{-\frac{2}{3}} p_{O_2}^{-\frac{1}{6}} \tag{6}$$

The charge carrier site fraction can be obtained indirectly from its proportionality to conductivity via the charge mobility or directly from the Seebeck coefficient as depicted in Figure 5. The two methods are independent and both datasets exhibit the characteristic slope of -1/6 in the double logarithmic Brouwer plot.

The transition temperature of 650°C from equilibrium to frozen-in region coincides with the onset of weight loss in the thermogravimetric measurement. Between 500°C to 900°C a fully reversible weight loss of 0.16 wt% is observable. Assuming this weight loss is solely due to the proposed formation of oxygen vacancies, 0.16 wt% correspond to an oxygen site fraction of $\Delta X_{v_{O3}^{\bullet\bullet}}$ = 0.039. Following the electroneutrality condition (2) this corresponds to a $\Delta X_{\mathrm{Fe^{2+}}}$=0.078, which is in close agreement with the charge carrier increase of $\Delta X_{\mathrm{Fe^{2+}}}$=0.068 in the equilibrium region, visible in Figure 7.

This typical behavior confirms our model on the formation of doubly charged oxygen vacancies as the source of the n-type charge carriers in form of reduced Fe^{2+} species in Fe_2WO_6 under equilibrium conditions. We can accordingly formulate the chemical sum formula as $Fe^{3+}{}_{2-X}Fe^{2+}{}_{X}WO_{6-X/2}$.

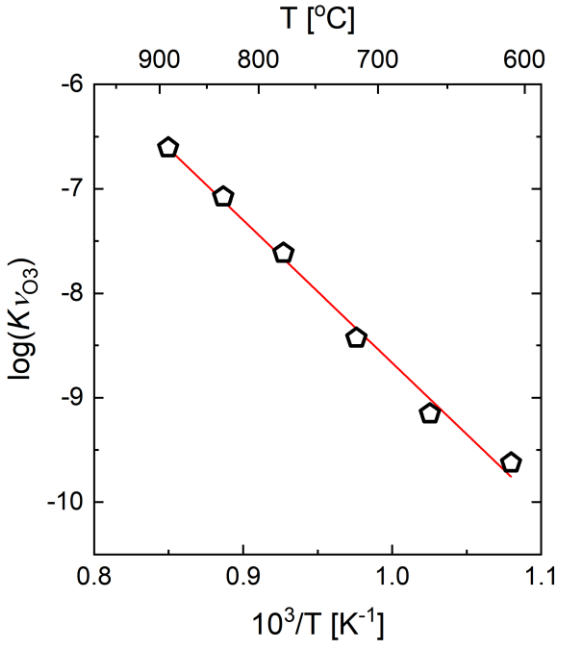

Figure 8: van 't Hoff plot of equilibrium coefficient versus inverse temperature. The equilibrium coefficient is obtained from equation (5) taking into account the electroneutrality as stated in equation (2).

We can now parameterize the defect chemical reaction (3) by expressing the temperature dependent equilibrium coefficient $K_{v_{O3}^{\bullet\bullet}}$ by means of the van 't Hoff equation, allowing us to extract the standard enthalpy of formation and the associated standard entropy change.

$$K_{v_{O3}^{\bullet\bullet}} = \exp\left(\frac{\Delta S_{v_{O3}^{\bullet\bullet}}^{\ominus}}{k}\right)\exp\left(-\frac{\Delta H_{v_{O3}^{\bullet\bullet}}^{\ominus}}{kT}\right) \tag{7}$$

From the van 't Hoff plot in Figure 8, we obtain a standard formation enthalpy of 113(5) kJmol^{-1} [1.18(5) eV] from the slope and a standard entropy change of 41(5) Jmol^{-1}K^{-1} from the intersect. The model established for the charge carrier concentration in equilibrium with oxygen, allows us to decouple the mobility from the conductivity and to describe it in a frame of thermally activated polaron hopping (u < 0.1 cm^{2}V^{-1}s^{-1}).[21] We use quantitative charge carrier concentrations for this via $n = 8X_{\mathrm{Fe}^{2+}}/V$ (V is the unit cell volume of 376.83 × 10^{-24} cm^{-3}).

$$\sigma = enu = enu_0\frac{1}{T}exp\left(-\frac{E_u}{k_BT}\right) \tag{8}$$

Here, e is the elemental charge, n the charger carrier concentration, and k_B Boltzmann's constant. E_u is the activation energy for hopping, u_0 is the mobility pre-factor. The mobility prefactor is dependent on whether the polaron hopping is adiabatic or non-adiabatic.

$$u_0 = \frac{zed^2\nu_{ph}}{2k_B} \qquad \text{Adiabatic}$$

$$u_0 = \frac{zed^2}{2k_B}\frac{J^2}{2h}\left(\frac{\pi}{4E_u k_B T}\right)^{\frac{1}{2}} \qquad \text{Non-adiabatic} \tag{9}$$

Here ν_{ph} denotes the maximum longitudinal phonon frequency, J the overlap integral, and z is the number of neighboring sites in jump distance d. We consider the Fe1-Fe1 distance of 3.097 Å to be the most relevant jump distance as it corresponds to the edge sharing octahedra along the crystallographic c-axis. The structure of hexagonal close packed oxygen with half of the octahedral voids filled, results in two nearest Fe neighbors ($z = 2$). By comparing the two mechanisms on the basis of the adiabatic parameter η_2, one can deduce the actual transport mechanism (η_2>1 for adiabatic, η_2<< for non-adiabatic). [22, 23]

$$\eta_2 = \frac{J^2}{h\nu_{ph}}\left(\frac{1}{E_u k_B T}\right)^{\frac{1}{2}} \tag{10}$$

The polaron hopping activation energy of E_u = 0.34(1) eV was obtained from the slope in the Arrhenius plot and is invariant in both the equilibrium- and frozen-in regions. In the frozen-in region E_u corresponds to the conductivity activation energy [E_σ^f = 0.35(1) eV from $\ln(\sigma T)$ vs $1/T$] and is in good agreement with previously reported values of 0.33 eV.[5] From the adiabatic mobility pre-exponential we estimate a maximum optical phonon frequency of ν_{ph} = 3.3(2) x 10^{13} Hz. No comparable phonon frequencies are available experimentally for Fe_2WO_6. However, the frequency lies rather close to typical maximum optical frequencies of Fe_2O_3 (1.9 x 10^{13} Hz) and WO_3 (3.23 x 10^{13} Hz).[24, 25] We obtain an overlap integral of $J = 0.28(1)$ eV from a $\ln(uT^{3/2})$ vs $1/T$ plot and conclude on an adiabatic polaron hopping, as the adiabatic parameter exceeds unity η_2>>1.

The mobility obtained from combination of charge carrier concentration with conductivity data is depicted as a function of inverse temperature in Figure 7, and a complete description of the mobility reads

$$u = 400(50)\ \mathrm{cm^2 KV^{-1}s^{-1}}\ \frac{1}{T}\exp\left(\frac{0.34(1)\ \mathrm{eV}}{k_B T}\right) \tag{11}$$

Furthermore, we may derive an expression for the conductivity in the equilibrium region that includes variable charge carrier concentration by combining equations (6), (7), and (8) (Absolute charge carrier concentrations in cm^{-3} are used). As only the mobility activation term and the enthalpy of formation term are temperature dependent, the conductivity activation

energy in the equilibrium region in Figure 2b is the sum of the activation energy for polaron hopping and the standard enthalpy of formation of oxygen vacancies

$$\sigma_{eq} = \frac{eu_0}{T}\frac{2^{\frac{1}{3}}8}{V}\left(\frac{g_{Fe^{2+}}}{g_{Fe^{3+}}}\right)^{-\frac{2}{3}} p_{O_2}^{-\frac{1}{6}} \exp\left(\frac{\Delta S_{v_{O_3}^{\cdot\cdot}}^{\ominus}}{3k}\right)\exp\left(\frac{-E_\sigma^{eq}}{kT}\right), \text{ with } E_\sigma^{eq} = \frac{\Delta H_{v_{O_3}^{\cdot\cdot}}^{\ominus}}{3} + E_u \quad (12)$$

From the conductivity activation energy E_σ^{eq} = 0.79(4) eV in the equilibrium region and with the polaron hopping activation energy E_u = 0.34(1) eV we estimate a standard enthalpy of formation of 130(15) kJmol^{-1} [1.35(15) eV]. The intersect allows for an estimate of the standard entropy change of 56(20) Jmol^{-1}K^{-1}, which is close to the empirically expected 60 Jmol^{-1}K^{-1} upon the release of half a mole of gaseous oxygen. The thermodynamic parameters from the conductivity analysis largely agree with those obtained from the charge carrier site fraction, albeit with higher standard deviations, since more terms are involved.

The relatively high conductivity, large Seebeck coefficient, and low thermal conductivity in addition to its remarkable stability towards temperature and oxidizing conditions, make Fe_2WO_6 an interesting n-type material for thermoelectric applications. The power factor ($\alpha^2\sigma$) increases exponentially with temperature, governed by the activated conductivity and reaches the highest observable value of 42 µWK^{-2}m^{-1} at 950°C. As the thermal conductivity stays low over the entire temperature range, the dimensionless figure of merit ($zT = \frac{\alpha^2\sigma}{\kappa}T$) follows the course of the power factor closely, as evident in Figure 9, reaching zT = 0.027 at 900°C. It should be noted that the samples in this study are undoped and that further improvements in the thermoelectric performance should be pursued by exploring doping of the system.

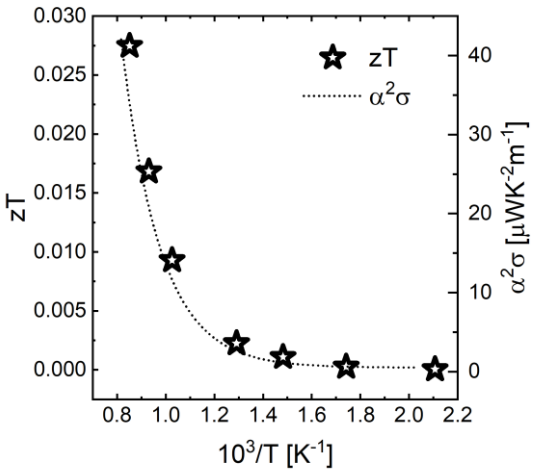

Figure 9: Dimensionless figure of merit ($zT = \frac{\sigma\alpha^2}{\kappa}T$) and power factor (PF= $\sigma\alpha^2$) in air as function of temperature for Fe_2WO_6.

Conclusions

In this work, we have established a defect chemical model to describe the electrical transport and the oxygen non-stoichiometry in Fe_2WO_6. Conductivity and Seebeck coefficient measurements concluded Fe_2WO_6 is an n-type conductor over the entire temperature and oxygen partial pressure ranges investigated. From detailed refinements of high quality synchrotron x-ray powder diffraction data, we could show that one of the oxygen sites (O3) is a preferred oxygen deficient site. Oxygen vacancies are compensated by reduced Fe^{2+} species, acting as charge carriers in an adiabatic polaron hopping manner. At high temperatures the material is in chemical equilibrium with atmospheric oxygen and forms oxygen vacancies and charge carriers with a standard formation enthalpy of 130(15) kJmol^{-1} and a corresponding standard change in entropy of 41(5) Jmol^{-1}K^{-1}. A freezing-in of oxygen vacancies below 650°C results in a region of constant charge carriers, with a Fe^{2+} site fraction of $X_{Fe^{2+}} \cong 0.03$. We show that the polaron hopping activation energy of 0.34(1) eV is constant across both regions, which reconciles the conductivity and chemical equilibrium model. We measure a low thermal conductivity for Fe_2WO_6, which was reported for the first time. The stability at high temperatures and oxidizing conditions makes Fe_2WO_6 a promising n-type thermoelectric oxide with a *zT* of 0.027 at 900°C.

Conflicts of interest

There are no conflicts of interest to declare.

References

1. Hoang, K., M. Oh, and Y.K. Choi, *Electronic structure, polaron formation, and functional properties in transition-metal tungstates.* Rsc Advances, 2018. **8**(8): p. 4191-4196.
2. Heyer, O., et al., *A new multiferroic material: MnWO4.* Journal of Physics-Condensed Matter, 2006. **18**(39): p. L471-L475.
3. Kumar, R.D. and S. Karuppuchamy, *Microwave-assisted synthesis of copper tungstate nanopowder for supercapacitor applications.* Ceramics International, 2014. **40**(8): p. 12397-12402.
4. Abdi, F.F., et al., *Assessing the Suitability of Iron Tungstate (Fe2WO6) as a Photoelectrode Material for Water Oxidation.* Journal of Physical Chemistry C, 2017. **121**(1): p. 153-160.
5. Bharati, R. and R.A. Singh, *The electrical properties of Fe2WO6.* Journal of Materials Science, 1981. **16**(2): p. 511-514.
6. Schrade, M., et al., *Versatile apparatus for thermoelectric characterization of oxides at high temperatures.* Rev Sci Instrum, 2014. **85**(10): p. 103906.
7. Ltd, C.S., *CasaXPS Version 2.3.19PR1.0*. Casa Software Ltd.
8. McCusker, L.B., et al., *Rietveld refinement guidelines.* Journal of Applied Crystallography, 1999. **32**(1): p. 36-50.
9. Sieber, K., et al., *Preparation and Properties of Substituted Iron Tungstates.* Journal of Solid State Chemistry, 1983. **47**(3): p. 361-367.
10. Leiva, H., K. Dwight, and A. Wold, *Preparation and Characterization of Conducting Iron Tungstates.* Journal of Solid State Chemistry, 1982. **42**(1): p. 41-46.
11. Soumendra Nath Panja, J.K., Luminita Harnagea, A. K. Nigam, and Sunil Nair, *Magnetic and dielectric investigations of γ - Fe2WO6.* 2017.
12. Yamashita, T. and P. Hayes, *Analysis of XPS spectra of Fe^{2+} and Fe^{3+} ions in oxide materials.* Applied Surface Science, 2008. **254**(8): p. 2441-2449.
13. M.BronoldY.TommW.Jaegermann, *Surface states on cubic d-band semiconductor pyrite (FeS2).* Surface Science, 1994. **314**(3).
14. Droubay, T. and S.A. Chambers, *Surface-sensitive Fe 2p photoemission spectra for α-Fe2O3: The influence of symmetry and crystal-field strength.* Physical Review B, 2001. **64**(20): p. 205414.
15. IRCHALLC, T., et al., *A study of iron-tungsten oxides and iron-chromium-tungsten oxides.*
16. Schmidbauer, E., U. Schanz, and F.J. Yu, *Electrical transport properties of mono- and polycrystalline FeWO4.* Journal of physics condensed Matter, 1991. **3**(3): p. 5341-5352.
17. Chaikin, P.M. and G. Beni, *Thermopower in the correlated hopping regime.* Physical Review B, 1976. **13**(2): p. 647-651.
18. Koshibae, W., K. Tsutsui, and S. Maekawa, *Thermopower in cobalt oxides.* Physical Review B, 2000. **62**(11): p. 6869-6872.
19. Guskos, N., et al., *Magnetic and EPR Studies of α-, β-, and γ-Fe2WO6 Phases at Low Temperatures.* Journal of Solid State Chemistry, 1995. **120**(2): p. 216-222.
20. Sieber, K., et al., *Preparation and photoelectronic properties of FeWO4.* Materials Research Bulletin, 1982. **17**(6): p. 721-725.
21. Austin, I.G. and N.F. Mott, *Polarons in Crystalline and Non-Crystalline Materials.* Advances in Physics, 1969. **18**(71): p. 41-+.
22. Casado, J.M., J.H. Harding, and G.J. Hyland, *Small-Polaron Hopping in Mott-Insulating Uo2.* Journal of Physics-Condensed Matter, 1994. **6**(25): p. 4685-4698.
23. Firsov, I.G.L.a.Y.A., *Kinetic theroy of semiconductors with low mobility.* J. Exptl. Theoret. Phys, 1963. **16**(5): p. 1843-1860.
24. Seinosuke Onari, T.A., Keiei Kudo, *Infrared lattice vibrations and dielectric dispersion in α-Fe203.* Physical Review B, 1977. **16**(4).

25. Ping, Y., D. Rocca, and G. Galli, *Optical properties of tungsten trioxide from first-principles calculations.* Physical Review B, 2013. **87**(16).